Deltahedral self-stabilized virtual elements for 3D linear elastostatics problems

Dexin Sun[a,b], Elias Pescialli[b], Qun Li[a], Massimiliano Cremonesi[b], Carlo Lovadina[d,e], Umberto Perego[b,*] and Alessandro Russo[c,d]

[a] *State Key Laboratory for Strength and Vibration of Mechanical Structures, School of Aerospace Engineering, Xi'an Jiaotong University, Xi'an 710049, China*

[b] *Department of Civil and Environmental Engineering, Politecnico di Milano, Milan 20133, Italy*

[c] *Department of Mathematics and Applications, Università di Milano-Bicocca, Milan I-20153, Italy*

[d] *IMATI-CNR, Pavia I-27100, Italy*

[e] *Department of Mathematics, Università di Milano, Milan 21033, Italy*

ARTICLE INFO

Keywords:
Self-stabilized virtual element
Deltahedral elements
Hu-Washizu variational approach
3D linear elastostatics
Virtual element method

ABSTRACT

The Virtual Element Method (VEM), a new generation of the traditional finite element method (FEM), allows for arbitrary polyhedral meshes, with elements not necessarily convex. However, the stiffness matrix of the Virtual Element (VE) in most cases requires stabilization, which is one of the main limitations of the VEM. This paper presents a new type of 3D self-stabilized VE, based on a Hu-Washizu variational approach for 3D linear elastostatics. The surface of the new element is composed of triangular faces, resembling the Greek letter Delta (Δ). Due to its unique geometric features, the new VE is named *Deltahedron element*. The advantage of triangles over faces of arbitrary polygonal shapes is that the displacement model is polynomial on the faces and therefore is not virtual. 8-node Deltahedra with 12 triangular faces are of particular interest as they can be smoothly coupled to a flat face of an 8-node 3D finite element (*brick element*). Numerical tests have been conducted on highly distorted, self-stabilized, deltahedral 8-node elements, including non-convex shapes, and they have shown good accuracy and expected convergence rates. The issue of integrals computation is also discussed in detail.

1. Introduction

The finite element method (FEM) is a widely used approach to solve boundary value problems. However, the traditional isoparametric FEM poses severe restrictions on the element shapes – it only allows for regularly-shaped elements, as overly distorted elements may lead to accuracy deterioration and even to a singular Jacobian [1] – making the meshing process time-consuming. The Virtual Element Method (VEM), proposed by Beirão da Veiga et al. [2, 3] as an extension of the traditional FEM, overcomes this issue by permitting the usage of arbitrarily shaped elements (not necessarily convex), with an accuracy insensitive to distortions, which can be smoothly integrated into an existing finite element mesh. In the past ten years, the VEM has been developed for many applications in mechanics, such as, e.g., in elastostatics [3, 4, 5, 6, 7, 8], elastodynamics [9, 10, 11, 12], contact problems [13, 14, 15, 16], fracture mechanics [17, 18, 19, 20]. See also the recent book [21] for a comprehensive and updated survey of VEM applications to engineering problems and the review in [22].

In the 2D VEM framework, displacement shape functions are explicitly known only on the element edges, where they are described by a polynomial of degree k (which represents the order of accuracy of the method). They are

*Corresponding author.
Email address: umberto.perego@polimi.it(U. Perego)

unknown inside the element, but their exact knowledge has been shown to be unnecessary to solve the problem [22]. This is why the VEM is called a *virtual* method, and the element space is referred to as the *virtual element space* [23]. In 3D, the element faces of an element of arbitrary shape and number of nodes are in general non-planar surfaces also for a first-order approximation. Even in the case of planar polygonal faces, the displacement shape functions are unknown on the element boundary. A special case is represented by solid elements with triangular faces, since in this case a displacement field on the face is explicitly defined by nodal values.

In most cases, the stiffness matrix of the Virtual Element (VE) requires stabilization to avoid zero-energy modes [24, 25, 26, 27]. In the standard displacement-based VEM formulation, the projection process assumes that the strain model is defined by a polynomial function of one order lower than the displacement shape functions [26]. This often results in a too-small strain space, and the element needs to be stabilized when the difference between the number of element Degrees Of Freedom (DOFs) and the strain parameters defining the strain model is greater than the number of rigid body modes [8]. The hourglass control technique [28, 24] is one of the most widely used stabilization methods. Although the stabilization term can make the element stiffness matrix have the correct singularity, it has some limitations. The stabilization process requires the definition of manually determined empirical parameters, without clear physical meaning [9]. To overcome this drawback, self-stabilized VEs, based on a mixed formulation, have been proposed in 2D [26, 29, 8, 30] and in 3D in [31]. For 3D problems (see also [32]), we propose a self-stabilized VEM based on a mixed Hu-Washizu variational formulation (see [33, 34] for the original formulation of the variational theorem), in the line of what proposed in [8] for 2D problems in the VEM context. Exploiting the independent definition of the strain model, the mixed formulation can naturally produce self-stabilized VEs, eliminating the need for a stabilization procedure. The basic idea is to enlarge the strain space by increasing the number of strain parameters.

In this work we consider a new type of $k = 1$ VE such that its surface is composed of an arbitrary number of triangles that resemble the Greek letter *Delta* (Δ), so this element is named *Deltahedron*. We focus in particular on 12-faces Deltahedra, which can be viewed as approximating the geometry of a hexahedron. The quadrilateral faces of a hexahedron are in general not planar and therefore cannot be treated with the standard VEM approach, which requires flat polygonal faces. The subdivision of a skew quadrilateral face into two triangles allows to overcome the problem. Furthermore, the displacement field on a triangular element face with three nodes is polynomial of order one and therefore is not virtual, greatly simplifying the VE formulation. To simplify the computation of the discretized compatibility operator, div-free strain models are considered, as proposed in [30] for 2D Poisson's problems and in [26] for 2D elastostatics. Several different self-stabilized deltahedral VEs based on the Hu-Washizu variational approach are implemented and tested for 3D linear elastostatics.

This paper is organized as follows. In Section 2, we briefly recall the Hu-Washizu finite element formulation for 3D linear elastostatics; in Section 3, we introduce the VEM formulation with deltahedral elements, including element de-

scription, investigated strain models, integration schemes, numerical check of element stability, and combination with standard brick finite elements; in Section 4, we conduct a series of numerical applications for the proposed VEs, containing convergence tests, other structural examples compared with the FEM, and a comparison of the computational efficiency of different integration schemes; in Section 5, we highlight the concluding remarks.

2. Hu-Washizu discrete formulation for 3D linear elastostatics

In this study, we focus on three-dimensional linear elasticity with small displacements and strains. Consider a linear elastic body occupying the 3D domain $\Omega \subset \mathbb{R}^3$, whose boundary $\partial\Omega$ contains two parts, namely $\partial_u\Omega$ and $\partial_p\Omega$, with $\partial_u\Omega \cup \partial_p\Omega = \partial\Omega$ and $\partial_u\Omega \cap \partial_p\Omega = \emptyset$. The body is subjected to body forces $\boldsymbol{b}$ in Ω, surface tractions $\boldsymbol{p}$ on $\partial_p\Omega$, and imposed displacements $\bar{\boldsymbol{u}}$ on $\partial_u\Omega$.

We adopt a three-field Hu-Washizu functional for the formulation of the elastostatic problem, assuming as independent variables displacements $\boldsymbol{u}$, strains $\boldsymbol{\varepsilon}$, and stresses $\boldsymbol{\sigma}$:

$$\Pi(\boldsymbol{u}, \boldsymbol{\varepsilon}, \boldsymbol{\sigma}) = \frac{1}{2}\int_\Omega \boldsymbol{\varepsilon}^T \boldsymbol{D}\boldsymbol{\varepsilon} d\Omega - \int_\Omega \boldsymbol{\sigma}^T (\boldsymbol{\varepsilon} - \boldsymbol{S}\boldsymbol{u})\, d\Omega - \int_\Omega \boldsymbol{u}^T \boldsymbol{b} d\Omega - \int_{\partial_p\Omega} \boldsymbol{u}^T \boldsymbol{p} ds \tag{1}$$

where it is assumed a priori $\boldsymbol{u} = \bar{\boldsymbol{u}}$ on $\partial_u\Omega$. In Eq. (1), $\boldsymbol{D}$ is the matrix of elastic constants and $\boldsymbol{S}$ is the compatibility differential operator, defined as:

$$\boldsymbol{S} = \begin{bmatrix} \partial_x & 0 & 0 \\ 0 & \partial_y & 0 \\ 0 & 0 & \partial_z \\ \partial_y & \partial_x & 0 \\ 0 & \partial_z & \partial_y \\ \partial_z & 0 & \partial_x \end{bmatrix} \tag{2}$$

where $\partial_{(\cdot)}$ denotes the partial derivative with respect to $(\cdot)$. Matrix notation for strains and stresses is adopted so that $\boldsymbol{\varepsilon}$ and $\boldsymbol{\sigma}$ are 6-component column vectors gathering strain and stress components, respectively.

We enforce the stationarity of the mixed functional to get the weak form of the governing equations:

$$\begin{aligned} \delta\Pi = &\int_\Omega \delta\boldsymbol{\varepsilon}^T \boldsymbol{D}\boldsymbol{\varepsilon} d\Omega - \int_\Omega \boldsymbol{\sigma}^T (\delta\boldsymbol{\varepsilon} - \boldsymbol{S}\delta\boldsymbol{u})\, d\Omega - \int_\Omega \delta\boldsymbol{\sigma}^T (\boldsymbol{\varepsilon} - \boldsymbol{S}\boldsymbol{u})\, d\Omega - \int_\Omega \delta\boldsymbol{u}^T \boldsymbol{b} d\Omega - \int_{\partial_p\Omega} \delta\boldsymbol{u}^T \boldsymbol{p} ds \\ &= 0 \qquad \forall \delta\boldsymbol{u}, \forall \delta\boldsymbol{\varepsilon}, \forall \delta\boldsymbol{\sigma} \end{aligned} \tag{3}$$

Integrating by parts the term $\int_\Omega \boldsymbol{\sigma}^T \boldsymbol{S}\delta\boldsymbol{u}d\Omega$:

$$\int_\Omega \boldsymbol{\sigma}^T \boldsymbol{S}\delta\boldsymbol{u}d\Omega = \int_{\partial\Omega} \delta\boldsymbol{u}^T \mathbb{N}\boldsymbol{\sigma}ds - \int_\Omega \delta\boldsymbol{u}^T \boldsymbol{S}^T\boldsymbol{\sigma}d\Omega \tag{4}$$

where $\mathbb{N}$ denotes the outward normal to the boundary:

$$\mathbb{N} = \begin{bmatrix} n_x & 0 & 0 & n_y & 0 & n_z \\ 0 & n_y & 0 & n_x & n_z & 0 \\ 0 & 0 & n_z & 0 & n_y & n_x \end{bmatrix} \tag{5}$$

one obtains the weak form of the governing equations:

$$\begin{aligned} \delta\Pi = &- \int_\Omega \delta\boldsymbol{u}^T \left(\boldsymbol{S}^T\boldsymbol{\sigma} + \boldsymbol{b}\right) d\Omega + \int_\Omega \delta\boldsymbol{\varepsilon}^T \left(\boldsymbol{D}\boldsymbol{\varepsilon} - \boldsymbol{\sigma}\right) d\Omega - \int_\Omega \delta\boldsymbol{\sigma}^T \left(\boldsymbol{\varepsilon} - \boldsymbol{S}\boldsymbol{u}\right) d\Omega + \int_{\partial_p\Omega} \delta\boldsymbol{u}^T \left(\mathbb{N}\boldsymbol{\sigma} - \boldsymbol{p}\right) ds \\ &= 0 \qquad \forall\delta\boldsymbol{u}, \forall\delta\boldsymbol{\varepsilon}, \forall\delta\boldsymbol{\sigma} \end{aligned} \tag{6}$$

A finite element discretization of Ω with n_e finite elements Ω_e is performed. A local non-dimensional coordinate system $\boldsymbol{\xi}$ is defined for each element

$$\boldsymbol{\xi} = \begin{bmatrix} \xi \\ \eta \\ \zeta \end{bmatrix} \tag{7}$$

with

$$\xi = \frac{x - x_G}{h_e},\ \eta = \frac{y - y_G}{h_e},\ \zeta = \frac{z - z_G}{h_e} \tag{8}$$

where x_G , y_G , and z_G are the Cartesian coordinates of the element centroid, and h_e is the element diameter.

An independent modeling of local displacements, strains and stresses is introduced:

$$\boldsymbol{u}(\boldsymbol{\xi}) \approx \boldsymbol{u}^h(\boldsymbol{\xi}) = \boldsymbol{N}_u(\boldsymbol{\xi})\hat{\boldsymbol{u}}, \quad \boldsymbol{\varepsilon}(\boldsymbol{\xi}) \approx \boldsymbol{\varepsilon}^h(\boldsymbol{\xi}) = \boldsymbol{N}_\varepsilon(\boldsymbol{\xi})\hat{\boldsymbol{\varepsilon}}, \quad \boldsymbol{\sigma}(\boldsymbol{\xi}) \approx \boldsymbol{\sigma}^h(\boldsymbol{\xi}) = \boldsymbol{N}_\sigma(\boldsymbol{\xi})\hat{\boldsymbol{\sigma}} \tag{9}$$

where $\hat{\boldsymbol{u}}$, $\hat{\boldsymbol{\varepsilon}}$, and $\hat{\boldsymbol{\sigma}}$ are vectors of displacement, strain, and stress parameters, respectively and $\boldsymbol{N}_u$, $\boldsymbol{N}_\varepsilon$, and $\boldsymbol{N}_\sigma$ are matrices of shape functions, defined in Ω_e, and of dimensions $3 \times n_u$, $6 \times n_\varepsilon$, and $6 \times n_\sigma$, respectively, where n_u, n_ε, and n_σ are the number of parameters describing the approximate displacement, strain and stress fields. Conservation

in the scalar product requires that:

$$\hat{\boldsymbol{\sigma}}^T \hat{\boldsymbol{\varepsilon}} = \int_{\Omega_e} \boldsymbol{\sigma}^T \boldsymbol{\varepsilon} d\Omega = \hat{\boldsymbol{\sigma}}^T \left(\int_{\Omega_e} \boldsymbol{N}_\sigma^T \boldsymbol{N}_\varepsilon d\Omega \right) \hat{\boldsymbol{\varepsilon}} \tag{10}$$

Eq. (10) implies that $n_\varepsilon = n_\sigma$ and that:

$$\int_{\Omega_e} \boldsymbol{N}_\sigma^T \boldsymbol{N}_\varepsilon d\Omega = \boldsymbol{I} \tag{11}$$

where $\boldsymbol{I}$ is the $n_\varepsilon \times n_\varepsilon$ identity matrix. A choice for the stress shape functions $\boldsymbol{N}_\sigma$ satisfying the above requirement is

$$\boldsymbol{N}_\sigma = \boldsymbol{N}_\varepsilon \left(\int_{\Omega_e} \boldsymbol{N}_\varepsilon^T \boldsymbol{N}_\varepsilon d\Omega \right)^{-1} = \boldsymbol{N}_\varepsilon \boldsymbol{G}^{-1} \tag{12}$$

where the square and invertible matrix $\boldsymbol{G}$ is:

$$\boldsymbol{G} = \int_{\Omega_e} \boldsymbol{N}_\varepsilon^T \boldsymbol{N}_\varepsilon d\Omega \tag{13}$$

Substituting the models in (9) in the expression (1) of the mixed functional and enforcing stationarity with respect to the discretization parameters $\hat{\boldsymbol{u}}$, $\hat{\boldsymbol{\varepsilon}}$, and $\hat{\boldsymbol{\sigma}}$, the stationarity conditions are obtained in the form

$$\partial_{\hat{\boldsymbol{u}}} \Pi_e^h = 0 \quad \Longrightarrow \quad \boldsymbol{C}^T \hat{\boldsymbol{\sigma}} = \boldsymbol{F}_e \tag{14}$$

$$\partial_{\hat{\boldsymbol{\varepsilon}}} \Pi_e^h = 0 \quad \Longrightarrow \quad \hat{\boldsymbol{\sigma}} = \boldsymbol{E} \hat{\boldsymbol{\varepsilon}} \tag{15}$$

$$\partial_{\hat{\boldsymbol{\sigma}}} \Pi_e^h = 0 \quad \Longrightarrow \quad \hat{\boldsymbol{\varepsilon}} = \boldsymbol{C} \hat{\boldsymbol{u}} \tag{16}$$

where the following quantities have been introduced:

(i) element elastic matrix

$$\boldsymbol{E} = \int_{\Omega_e} \boldsymbol{N}_\varepsilon^T \boldsymbol{D} \boldsymbol{N}_\varepsilon d\Omega \tag{17}$$

(ii) element compatibility matrix

$$\boldsymbol{C} = \int_{\Omega_e} \boldsymbol{N}_\sigma^T \left(\boldsymbol{S} \boldsymbol{N}_u \right) d\Omega = \boldsymbol{G}^{-1} \int_{\Omega_e} \boldsymbol{N}_\varepsilon^T \left(\boldsymbol{S} \boldsymbol{N}_u \right) d\Omega = \boldsymbol{G}^{-1} \boldsymbol{A} \tag{18}$$

with

$$\boldsymbol{A} = \int_{\Omega_e} \boldsymbol{N}_{\varepsilon}^{T} \left(\boldsymbol{S} \boldsymbol{N}_{u} \right) d\Omega \tag{19}$$

(iii) element equivalent forces vector

$$\boldsymbol{F}_e = \int_{\Omega_e} \boldsymbol{N}_u^T \boldsymbol{b} d\Omega + \int_{\partial_p \Omega_e} \boldsymbol{N}_u^T \boldsymbol{p} ds = \boldsymbol{F}_e^b + \boldsymbol{F}_e^p \tag{20}$$

Replacing Eq.(16) in Eq.(15) and Eq.(15) in Eq.(14), one obtains:

$$\boldsymbol{K}_e^c \hat{\boldsymbol{u}} = \boldsymbol{F}_e \tag{21}$$

where

$$\boldsymbol{K}_e^c = \boldsymbol{C}^T \boldsymbol{E} \boldsymbol{C} \tag{22}$$

is the consistent part of the element stiffness matrix. If the dimension of the kernel of $\boldsymbol{K}_e^c$ is greater than 6, i.e. greater than the number of the 3D rigid body modes, zero-energy modes (the so-called *hourglass modes*) can arise and $\boldsymbol{K}_e^c$ needs to be stabilized.

Once the displacement parameters $\hat{\boldsymbol{u}}$ have been computed by Eq.(21), the proposed mixed functional offers a straightforward way for stress and strain recovery. The approximate strain field and stress field of the VE can be respectively obtained as:

$$\boldsymbol{\varepsilon}^h = \boldsymbol{N}_{\varepsilon} \hat{\boldsymbol{\varepsilon}} = \boldsymbol{N}_{\varepsilon} \boldsymbol{C} \hat{\boldsymbol{u}}, \quad \boldsymbol{\sigma}^h = \boldsymbol{D} \boldsymbol{\varepsilon}^h = \boldsymbol{D} \boldsymbol{N}_{\varepsilon} \boldsymbol{C} \hat{\boldsymbol{u}} \tag{23}$$

3. Virtual element formulation with deltahedral elements

3.1. Element description

The general formulation in Section 2 will be exploited here to construct deltahedral elements based on the VEM. Let Ω_e denote the domain of a Deltahedron that is characterized by:

(i) a polyhedral shape, not necessarily convex;

(ii) an arbitrary number N_v of vertices;

(iii) an outer surface made of triangular faces.

A deltahedral element is shown in Fig. 1 with its triangular faces. In this paper, we focus on a particular type of

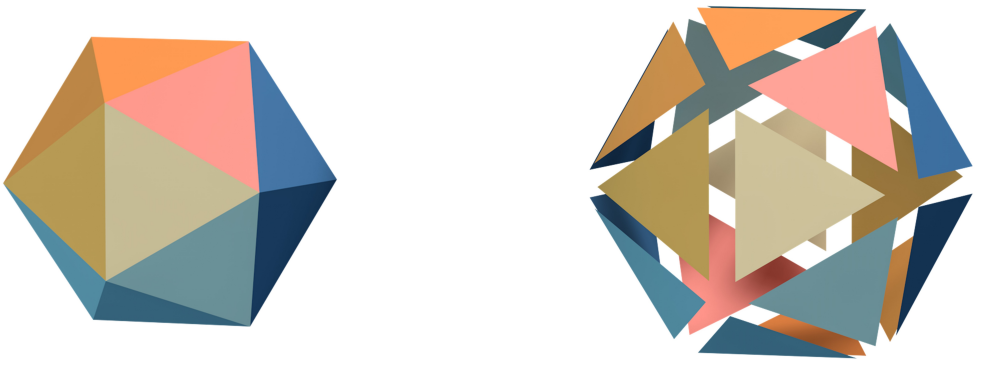

Fig. 1: Generic polyhedral deltahedral element and its triangular faces.

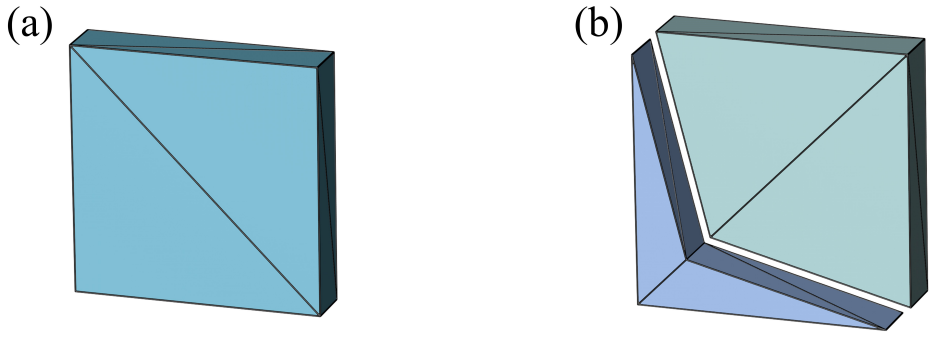

Fig. 2: Examples of brick-like (8 nodes) deltahedral elements used in this study. Each quadrilateral face of the brick is subdivided into two triangles: (a) brick-shaped Deltahedron, (b) pair of brick-like deltahedral elements: lower element with non-convex front and rear faces; upper element with convex faces.

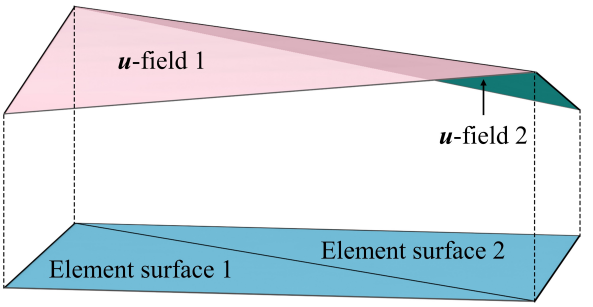

Fig. 3: Displacement field defined on two triangular faces corresponding to a quadrilateral face of a brick-like deltahedral element.

brick-like deltahedra with 8 vertices and 12 triangular faces, which can be thought of as being obtained from (possibly skew) hexahedra (*brick elements*), by dividing each of the six faces of the brick into two triangles using a diagonal, as shown in Fig. 2. It should be noted that a general brick element may have non-planar quadrilateral faces, so that talking about diagonals would be not completely appropriate. However, this rough description may help to better understand the geometry of the considered VEs.

Fig. 2(a) portrays a brick-shaped Deltahedron with 8 nodes and 12 triangular faces, while Fig. 2(b) shows a pair

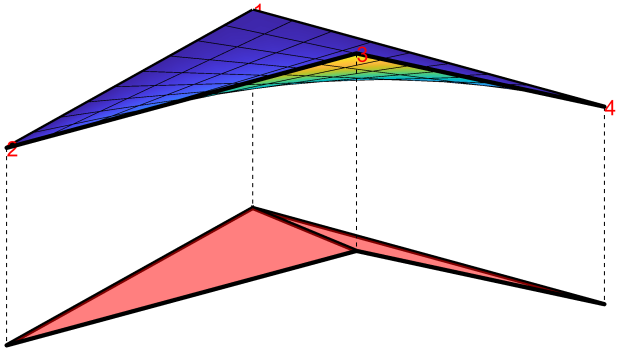

Fig. 4: Deltahedral VE brick-like face geometry (below) vs FEM bilinear face (above).

of brick-like VEs, the lower one non-convex and the upper one convex, with 8 nodes and 12 triangular faces each. It is worth noting that the diagonal lines of opposite rectangular faces are parallel, and that a maximum of two diagonal lines depart from each vertex.

In the VEM, the displacement shape functions $\boldsymbol{N}_u$ are not explicitly known inside the element. The displacement model is assumed to contain polynomials of degree k plus other unknown functions whose exact knowledge is not necessary to solve the problem. For this reason, an element of this kind is referred to as a virtual element. Using triangular faces with nodes in the vertices, as discussed above, is that the displacement model on the element faces is polynomial of order one (see Fig 3) and therefore is not virtual, while it remains virtual in the element interior.

A key property of the Virtual Element Method is its compatibility with the classical Finite Element Method, i.e. the possibility of considering Virtual Elements and Finite Elements in the same mesh. In principle, in view of their higher computational cost, Virtual Elements should be employed only when some extra features are needed. In the case under examination, the degrees of freedom of the 8-node Deltahedra and of the 8-node isoparametric brick elements are the same, hence it is possible to glue them together through the edges. The Deltahedron comes into play when the 8-node brick becomes too degenerate and the trilinear isoparametric map is no longer invertible. The face of the 8-node isoparametric brick and the face of the Deltahedron are different (Fig. 4): the first one is a bilinear surface while the second one is the union of two triangles. However, if the element curvature is small, the difference is negligible, taking into account that we are considering a linear approximation, ensuring a seamless transition between isoparametric bricks and Deltahedra.

The key operator in the present VEM formulation is the compatibility matrix $\boldsymbol{C}$ defined in Eq. (18), in which the matrix $\boldsymbol{G}$ is directly computable once the strain shape functions $\boldsymbol{N}_\varepsilon$ are defined. The computation of the matrix $\boldsymbol{A}$ is less straightforward, since its expression contains the matrix of displacements shape functions $\boldsymbol{N}_u$, unknown in the

element interior. To overcome the problem, one can integrate $\boldsymbol{A}$ by parts:

$$\boldsymbol{A} = \int_{\Omega_e} \boldsymbol{N}_\varepsilon^T \left(\boldsymbol{S}\boldsymbol{N}_u\right) d\Omega = \int_{\partial\Omega_e} \left(\mathbb{N}\boldsymbol{N}_\varepsilon\right)^T \boldsymbol{N}_u ds - \int_{\Omega_e} \left(\boldsymbol{S}^T\boldsymbol{N}_\varepsilon\right)^T \boldsymbol{N}_u d\Omega = \boldsymbol{A}_1 + \boldsymbol{A}_2 \tag{24}$$

The first term $\boldsymbol{A}_1$ in Eq. (24) results from the boundary integral of known quantities, as the matrix $\boldsymbol{N}_u$ is explicit on the boundary. The integral in the second term $\boldsymbol{A}_2$ has to be computed over the element interior, where the displacement model $\boldsymbol{N}_u$ is unknown. However, in the special cases that the strain model $\boldsymbol{N}_\varepsilon$ is constant or divergence-free, the first part $\boldsymbol{S}^T\boldsymbol{N}_\varepsilon$ of the integrand in $\boldsymbol{A}_2$ vanishes and one has $\boldsymbol{A} = \boldsymbol{A}_1$.

The element elastic matrix $\boldsymbol{E}$ defined in (17) is also computable, because it depends on the known strain shape functions $\boldsymbol{N}_\varepsilon$ and on the matrix $\boldsymbol{D}$ of elastic constants. Once the compatibility matrix $\boldsymbol{C}$ and the elastic matrix $\boldsymbol{E}$ have been computed, the local VEM consistent stiffness matrix $\boldsymbol{K}_e^c$ can be determined by Eq. (22).

3.2. Investigated strain models

In this paper, the displacement model is assumed to be linear on the boundary of each element, that is $k = 1$. Exploiting the adopted Hu-Washizu variational formulation, the strain models are chosen to be divergence-free (see also [26, 30]), so that $\boldsymbol{A}_2 = \boldsymbol{0}$ in Eq. (24) and $\boldsymbol{A} = \boldsymbol{A}_1$ is easily computable. In addition, as discussed in [8], the freedom offered by the mixed formulation allows to select strain models leading to self-stabilized consistent stiffness matrices $\boldsymbol{K}_e^c$. Even though this is not the case of the constant strain model, for which stabilization is required, this is discussed first, since it is the standard model in the presence of a $k = 1$ method, and we use it as a reference for the subsequent, higher order strain models.

The matrix $\boldsymbol{N}_\varepsilon$ of constant strain shape functions, shown below, requires only six strain parameters $\hat{\boldsymbol{\varepsilon}}$:

$$\boldsymbol{N}_\varepsilon = \begin{bmatrix} 1 & 0 & 0 & 0 & 0 & 0 \\ 0 & 1 & 0 & 0 & 0 & 0 \\ 0 & 0 & 1 & 0 & 0 & 0 \\ 0 & 0 & 0 & 1 & 0 & 0 \\ 0 & 0 & 0 & 0 & 1 & 0 \\ 0 & 0 & 0 & 0 & 0 & 1 \end{bmatrix} \tag{25}$$

Each element has 24 nodal displacement DOFs. Hourglass stabilization is therefore needed because the discrepancy between the number of the 24 DOFs and of the 6 strain parameters is greater than the number of the 6 3D rigid body modes. The hourglass stabilization discussed in [8] is used here and the reader is referred to there for the details.

The first immediate choice for achieving self-stability is, therefore, to increase the polynomial order of the strain

model and, consequently, the number of strain parameters. A complete polynomial strain model of order 1 is defined by 24 parameters and by the matrix $\boldsymbol{N}_{\boldsymbol{\varepsilon}}$ shown in Eq. (26) below:

$$\boldsymbol{N}_{\boldsymbol{\varepsilon}} = \begin{bmatrix} 1 & 0 & 0 & 0 & 0 & 0 & \xi & 0 & 0 & 0 & 0 & 0 & \eta & 0 & 0 & 0 & 0 & 0 & \zeta & 0 & 0 & 0 & 0 & 0 \\ 0 & 1 & 0 & 0 & 0 & 0 & 0 & \xi & 0 & 0 & 0 & 0 & 0 & \eta & 0 & 0 & 0 & 0 & 0 & \zeta & 0 & 0 & 0 & 0 \\ 0 & 0 & 1 & 0 & 0 & 0 & 0 & 0 & \xi & 0 & 0 & 0 & 0 & 0 & \eta & 0 & 0 & 0 & 0 & 0 & \zeta & 0 & 0 & 0 \\ 0 & 0 & 0 & 1 & 0 & 0 & 0 & 0 & 0 & \xi & 0 & 0 & 0 & 0 & 0 & \eta & 0 & 0 & 0 & 0 & 0 & \zeta & 0 & 0 \\ 0 & 0 & 0 & 0 & 1 & 0 & 0 & 0 & 0 & 0 & \xi & 0 & 0 & 0 & 0 & 0 & \eta & 0 & 0 & 0 & 0 & 0 & \zeta & 0 \\ 0 & 0 & 0 & 0 & 0 & 1 & 0 & 0 & 0 & 0 & 0 & \xi & 0 & 0 & 0 & 0 & 0 & \eta & 0 & 0 & 0 & 0 & 0 & \zeta \end{bmatrix} \tag{26}$$

This linear strain model would generate a 24×24 matrix $\boldsymbol{A}_1$ of rank 18, which would lead to rank$(\boldsymbol{K}_e^c) = 18$. However, the strain field in Eq. (26) is not divergence-free and matrix $\boldsymbol{A}_2$ in Eq. (24) does not vanish. The computation of $\boldsymbol{A}_2$ requires the introduction of 3 extra moments DOFs (see [8] for the details), and the gap between the rank of $\boldsymbol{K}_e^c$ (18) and the number of displacement DOFs (27) would become greater than the six rigid body motions, giving rise to three possible hourglass modes.

A second choice is to make the linear strain field divergence-free, as shown in Eq. (27) below, so that no additional DOFs are needed:

$$\boldsymbol{N}_{\boldsymbol{\varepsilon}} = \begin{bmatrix} 1 & 0 & 0 & 0 & 0 & 0 & 0 & 0 & 0 & \eta & 0 & 0 & \zeta & 0 & 0 \\ 0 & 1 & 0 & 0 & 0 & 0 & \xi & 0 & 0 & 0 & 0 & 0 & 0 & \zeta & 0 \\ 0 & 0 & 1 & 0 & 0 & 0 & 0 & \xi & 0 & 0 & \eta & 0 & 0 & 0 & 0 \\ 0 & 0 & 0 & 1 & 0 & 0 & 0 & 0 & 0 & 0 & 0 & 0 & 0 & 0 & \zeta \\ 0 & 0 & 0 & 0 & 1 & 0 & 0 & 0 & \xi & 0 & 0 & 0 & 0 & 0 & 0 \\ 0 & 0 & 0 & 0 & 0 & 1 & 0 & 0 & 0 & 0 & 0 & \eta & 0 & 0 & 0 \end{bmatrix} \tag{27}$$

However, the addition of the divergence-free condition implies reducing the number of strain parameters to 15, still giving rise to three possible hourglass modes. Indeed, adding linear parameters preserving the divergence-free property, would mean adding a linear combination of the parameters already included in the complete field of Eq. (26), which would not restore the rank of $\boldsymbol{A}_1$.

To overcome these problems and achieve a self-stabilized, $k = 1$, 8-node Deltahedron, three divergence-free 2^{nd}-degree polynomial strain fields are proposed and tested. Clearly, these fields will not be complete second order polynomials, as some parameters have to be suppressed to satisfy the condition $\boldsymbol{S}^{\mathrm{T}}\boldsymbol{N}_{\boldsymbol{\varepsilon}} = \boldsymbol{0}$ in (24), which is enforced to avoid the need of additional DOFs.

3.2.1. A 31 parameter quadratic strain scheme

The strain model of this scheme is obtained using a kind of *Airy function approach*. More precisely, we consider a complete 4^{th}-degree polynomial $\phi(\xi,\eta,\zeta)$, thus depending on 35 free parameters. Then, strains are computed as:

$$\boldsymbol{\varepsilon}(\xi,\eta,\zeta)=\begin{bmatrix}\varepsilon_x(\xi,\eta,\zeta)\\ \varepsilon_y(\xi,\eta,\zeta)\\ \varepsilon_z(\xi,\eta,\zeta)\\ \gamma_{xy}(\xi,\eta,\zeta)\\ \gamma_{yz}(\xi,\eta,\zeta)\\ \gamma_{xz}(\xi,\eta,\zeta)\end{bmatrix}=\begin{bmatrix}\phi_{,\eta\eta}+\phi_{,\zeta\zeta}\\ \phi_{,\xi\xi}+\phi_{,\zeta\zeta}\\ \phi_{,\xi\xi}+\phi_{,\eta\eta}\\ -\phi_{,\xi\eta}\\ -\phi_{,\eta\zeta}\\ -\phi_{,\xi\zeta}\end{bmatrix} \tag{28}$$

We notice that the constant and linear part of $\phi(\xi,\eta,\zeta)$ does not enter into play in (28), since second order derivatives are considered. Therefore only 31 parameters, out of the 35, are actually involved, leading to the following 6×31 strain matrix, whose entries are polynomials of degree at most 2:

$$\boldsymbol{N}_\varepsilon=\begin{bmatrix}
1&0&0&0&0&0&0&\eta&\zeta&0&0&\xi&\zeta&\xi&\eta&0&0&\eta^2&\zeta^2&0&0&2\xi\eta&2\eta\zeta&2\xi\zeta&2\eta\zeta&\xi^2&\eta^2{+}\zeta^2&\xi^2&0&2\xi\zeta&2\xi\eta\\
0&1&0&0&0&0&\xi&0&\zeta&\eta&\zeta&0&0&\xi&\eta&0&\xi^2&0&\zeta^2&2\xi\eta&2\xi\zeta&0&0&2\xi\zeta&2\eta\zeta&\eta^2&\eta^2&\xi^2{+}\zeta^2&2\eta\zeta&0&2\xi\eta\\
0&0&1&0&0&0&\xi&\eta&0&\eta&\zeta&\xi&\zeta&0&0&0&\xi^2&\eta^2&0&2\xi\eta&2\xi\zeta&2\xi\eta&2\eta\zeta&0&0&\xi^2{+}\eta^2&\zeta^2&\zeta^2&2\eta\zeta&2\xi\zeta&0\\
0&0&0&1&0&0&0&0&0&-\xi&0&-\eta&0&0&0&\zeta&0&0&0&-\xi^2&0&-\eta^2&0&0&0&-2\xi\eta&0&0&-2\xi\zeta&-2\eta\zeta&-\zeta^2\\
0&0&0&0&1&0&0&0&0&0&0&0&-\zeta&\xi&0&0&0&0&0&0&0&-\eta^2&0&-\zeta^2&0&-2\eta\zeta&0&-\xi^2&-2\xi\eta&-2\xi\zeta\\
0&0&0&0&0&1&0&0&0&0&-\xi&0&0&-\zeta&0&\eta&0&0&0&0&0&0&0&-\zeta^2&0&0&0&-2\xi\zeta&-2\xi\eta&-\eta^2&-2\eta\zeta
\end{bmatrix} \tag{29}$$

By construction, the above strains are divergence-free, so that the matrix $\boldsymbol{A}_2$ vanishes, cf. (24), and no additional DOFs are required for the displacement field.

Since the Deltahedron has 24 displacement DOFs, the 35 strain parameters are more than the minimum (not necessarily sufficient) to avoid the insurgence of hourglass modes. In this case, the VE is said to be *internally redundant*. In the applications, this VE will be referred to as ΔVEM8SS31-24DOFs (Deltahedron-VEM-8 nodes-Self-Stabilized-31 strain parameters-24DOFs).

Even though no stabilization should be needed for the element generated by Eq.(29), having a polynomial strain field made by 31 parameters leads to extensive computations, both for the entries of matrix $\boldsymbol{A}_1$, where monomials up to degree 3 have to be integrated (resulting from the 2^{nd}-degree strain field and 1^{st}-degree polynomial projection of the displacement field) and for matrices $\boldsymbol{G}$ and $\boldsymbol{E}$, where the integrands are monomials up to order 4. Therefore, a reduction of the number of strain field parameters is desirable.

3.2.2. A 25 parameter quadratic strain scheme

The strain model of this scheme exhibits the following features.

1. As for the previous case, polynomials of degree at most 2 are used for the strain components, but with a limited

number of free parameters;

2. the strain field is divergence-free;

3. the strain field is the symmetric gradient of some displacement field, whose components are then polynomials of degree at most 3.

To this end, we employ some results from the differential complex theory for elasticity problems, see for instance [35]. The construction is performed along the following line. We start considering a complete 4^{th}-degree polynomial $\phi(\xi,\eta,\zeta)$, thus depending on 35 free parameters; using $\phi(\xi,\eta,\zeta)$ we define the isotropic second order tensor $\boldsymbol{P} = \phi(\xi,\eta,\zeta)\,\boldsymbol{I}$. Then, we apply the *incompatibility* operator inc to obtain a second order tensor $\boldsymbol{Q}$ defined by $\boldsymbol{Q} = \text{inc}(\boldsymbol{P}) = \nabla\times\boldsymbol{P}\times\nabla$, where $\nabla\times$ and $\times\nabla$ respectively denote the column-wise curl and the row-wise curl of a second order tensor. By construction, see [35], $\boldsymbol{Q}$ is a divergence-free tensor whose entries are polynomials of degree at most 2. Of course, $\boldsymbol{Q}$ is not necessarily the symmetric gradient of any displacement field. However, see [35] again, there exists a vector field whose symmetric gradient is $\boldsymbol{Q}$ if and only if $\text{inc}(\boldsymbol{Q}) = 0$. We thus consider that subspace of all

$$\boldsymbol{Q} = \nabla\times(\phi(\xi,\eta,\zeta)\,\boldsymbol{I})\times\nabla \quad \text{such that} \quad \text{inc}(\boldsymbol{Q}) = 0\,,$$

where $\phi(\xi,\eta,\zeta)$ ranges over all the polynomials of degree at most 4. This is a subspace of dimension 25; a basis is given by the column of the following matrix.

$$\boldsymbol{N}_\varepsilon = \begin{bmatrix}
1&0&0&0&0&0&0&0&\xi&0&\xi&\eta&\zeta&\eta&\zeta & -2\xi^2+\eta^2+\zeta^2 & -2\xi\eta & -2\xi\zeta & 0 & 0 & \eta^2-\zeta^2 & 2\eta\zeta & 2\eta\zeta & -\eta^2+\zeta^2\\
0&1&0&0&0&0&\xi&\eta&\zeta&0&0&\xi&0&0&\eta&\zeta & \xi^2-\zeta^2 & 0 & 2\xi\zeta & -2\xi\eta & 2\xi\zeta & \xi^2-2\eta^2+\zeta^2 & -2\eta\zeta & 0 & -\xi^2+\zeta^2\\
0&0&1&0&0&0&\xi&\eta&\zeta&0&0&\eta&\zeta&0&0&\zeta & \xi^2-\eta^2 & 2\xi\eta & 0 & 2\xi\eta & -2\xi\zeta & -\xi^2+\eta^2 & 0 & -2\eta\zeta & \xi^2+\eta^2-2\zeta^2\\
0&0&0&1&0&0&0&-\xi&0&-\eta&\zeta&0&0&0&0&0 & 2\xi\eta & -\xi^2+\zeta^2 & 2\eta\zeta & -\eta^2+\zeta^2 & 2\eta\zeta & 2\xi\eta & 2\xi\zeta & 2\xi\zeta & -2\xi\eta\\
0&0&0&0&1&0&0&0&0&0&0&-\eta&-\zeta&0 & -2\eta\zeta & 2\xi\zeta & 2\xi\eta & 2\xi\zeta & 2\xi\eta & 2\eta\zeta & \xi^2-\eta^2 & \xi^2-\zeta^2 & 2\eta\zeta\\
0&0&0&0&0&1&0&0&-\xi&0&\eta&-\zeta&0&0&0&0 & 2\xi\zeta & 2\eta\zeta & -\xi^2+\eta^2 & 2\eta\zeta & \eta^2-\zeta^2 & -2\xi\zeta & 2\xi\eta & 2\xi\eta & 2\xi\zeta
\end{bmatrix} \tag{30}$$

Also in this case, the strain parameters are more than the minimum required and the element is internally redundant. In the applications, this VE will be referred to as ΔVEM8SS25-24DOFs

It should be noted that the 31 parameter quadratic model (29) can be obtained by means of an approach similar to the one used for (30). More precisely, still starting from the isotropic second order tensor $\boldsymbol{P} = \phi(\xi,\eta,\zeta)\,\boldsymbol{I}$, where $\phi(\xi,\eta,\zeta)$ is a generic 4^{th}-degree polynomial, the strains in (29) are exactly described by $\boldsymbol{Q} = \text{inc}(\boldsymbol{P})$.

3.2.3. An 18 parameter quadratic strain scheme

The third quadratic strain field shown in Eq. (31) is defined by 18 parameters - the minimum to suppress the rank deficiency caused by the shortage of strain parameters with respect to the 24 displacement parameters. It is derived by adding to the divergence-free 15-parameter linear field of Eq. (27) three other parameters obtained as a combination of the 31-parameters field of Eq. (28). More precisely, the 16^{th} parameter is obtained by summing the 4^{th} and 6^{th}

column of the 2nd-degree part of Eq. (28), the 17th parameter is obtained by summing the 7th and 9th column and the 18th parameter is obtained by summing the 5th and 8th column. The corresponding VE arising from this field will be denoted as ΔVEM8SS18-24DOFs, referring to an 8-node self-stabilized deltahedral VE with 18 strain parameters and 24 degrees of freedom.

$$\boldsymbol{N}_{\varepsilon} = \begin{bmatrix} 1 & 0 & 0 & 0 & 0 & 0 & 0 & 0 & 0 & \eta & 0 & 0 & \zeta & 0 & 0 & 2\xi\eta & 4\eta\zeta & 2\xi\zeta \\ 0 & 1 & 0 & 0 & 0 & 0 & \xi & 0 & 0 & 0 & 0 & 0 & 0 & \zeta & 0 & 2\xi\eta & 2\eta\zeta & 4\xi\zeta \\ 0 & 0 & 1 & 0 & 0 & 0 & 0 & \xi & 0 & 0 & \eta & 0 & 0 & 0 & 0 & 4\xi\eta & 2\eta\zeta & 2\xi\zeta \\ 0 & 0 & 0 & 1 & 0 & 0 & 0 & 0 & 0 & 0 & 0 & 0 & 0 & 0 & \zeta & -\xi^2-\eta^2 & 0 & 0 \\ 0 & 0 & 0 & 0 & 1 & 0 & 0 & 0 & \xi & 0 & 0 & 0 & 0 & 0 & 0 & 0 & -\eta^2-\zeta^2 & 0 \\ 0 & 0 & 0 & 0 & 0 & 1 & 0 & 0 & 0 & 0 & 0 & \eta & 0 & 0 & 0 & 0 & 0 & -\xi^2-\zeta^2 \end{bmatrix} \tag{31}$$

It is important to observe that there is a significant difference between the first two strain models (29)-(30) and the last one (31). The first two are obtained by the application of coordinate-free operators to complete polynomials; hence the resulting strains transform as a second-order tensor and consequently the obtained elements are frame-indifferent. In contrast, the third strain model is empirically defined in terms of local coordinates and the resulting element is not frame-indifferent. Therefore, the displacement solution in general depends on the mesh orientation, while preserving the first-order convergence rate. This drawback could be faced by adopting a 3D corotational definition of the intrinsic coordinates (ξ, η, ζ) as done e.g. in 2D in [36, 37].

3.3. Integration schemes

The numerical computation of volume integrals is a crucial step in the VEM procedure. This is achieved using the subdivision technique, wherein a Deltahedron is subdivided into several tetrahedra. The element compatibility matrix $\boldsymbol{G}$, element elastic matrix $\boldsymbol{E}$, and element equivalent nodal forces vector $\boldsymbol{F}_e$ are all computed using this process. The subdivision technique begins by dividing a deltahedral element, which can be a brick-like Deltahedron, a convex Deltahedron, or a non-convex Deltahedron, into two triangular prisms, which are then further divided into three tetrahedra each, as depicted in Fig. 5. The resulting tetrahedra are then integrated using Gaussian quadrature. The Gauss integration points in a unit tetrahedra are shown in Table 1 [38]. Finally, the integrals over each tetrahedron are summed to obtain the result over each deltahedral element.

We need to integrate two matrices, $\boldsymbol{G}$ and $\boldsymbol{E}$, over the volume for the constant, linear, and quadratic strain models. In the case of constant strain models, the matrices $\boldsymbol{G}$ and $\boldsymbol{E}$ are integrals of constant matrices, which require only one Gauss point per tetrahedron for accurate integration; in the case of linear strain models, the matrices $\boldsymbol{G}$ and $\boldsymbol{E}$ are integrals of quadratic polynomials, necessitating four Gauss points per tetrahedron for accurate integration; in the case of quadratic strain models, the matrices $\boldsymbol{G}$ and $\boldsymbol{E}$ are integrals of fourth-order polynomials, requiring eleven Gauss

points per tetrahedron for accurate integration. It is worth noting that in the present study, the integrand of matrix $\boldsymbol{F}$ is not purely polynomial. Nevertheless, even though a single Gauss point could be used without spoiling the convergence rate, we opted to use for integration the same Gauss points as those used for the matrices $\boldsymbol{G}$ and $\boldsymbol{E}$. This approach was found to provide satisfactory integration accuracy.

In the computation of the $\boldsymbol{A}_1$ matrix, the integration over the element boundary can be expressed as the sum of the integrals over the surface of each triangle. Table 2 [1] shows the Gauss integration points in a unit triangle. For the constant strain model, only one Gauss point is required per triangle since the matrix $\boldsymbol{A}_1$ are integrals of linear polynomials; for linear strain models, three Gauss points are required per triangle since the matrix $\boldsymbol{A}_1$ are integrals of quadratic polynomials; for quadratic strain models, four points are required per triangle to ensure integration accuracy as the matrix $\boldsymbol{A}_1$ are integrals of third-order polynomials. To sum up, Table 3 shows the varying number of integration points used in the convergence test with different strain models.

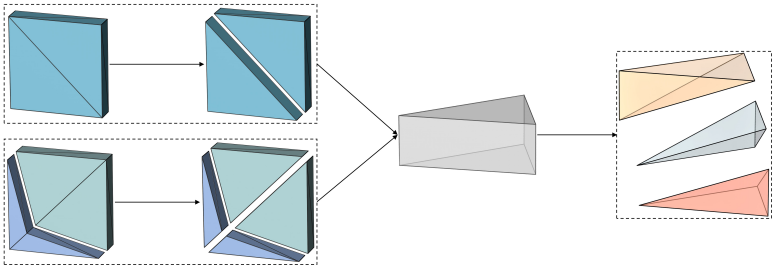

Fig. 5: Subdivision technique of deltahedral elements for volume integral.

A second approach has been implemented and tested, following a recursive algorithm presented in [39], which is a quadrature-free[1] integration scheme developed *ad hoc* to build stiffness matrices for discontinuous Galerkin methods on general polytopal meshes. The algorithm is a recursive call with a-priori exponential-time complexity with respect to the order of the monomial integrand, also depending on the number of lower order N-polytopes, i.e., the number of faces, edges, and vertices. However, a clever choice of the local reference frame for each N-polytope allows for drastically reduced computation times. In the algorithm, $\boldsymbol{x}_0 = (x_{0,1}, \dots, x_{0,d})$ is the origin of the reference system for the N-polytope $\mathcal{E}$ called as input parameter, and d_i is the algebraic distance between the sub $(N-1)$-polytope $\mathcal{E}_i$ and $\boldsymbol{x}_0$. The choice of $\boldsymbol{x}_0$ turns out to be critical. If $\boldsymbol{x}_0$ is selected such that one or more of its coordinates are 0, then the recursion calls for those components are not needed. In the implemented version this should be extensively exploited, considering also the degree of the variables making up the monomial being integrated: the coordinate of $\boldsymbol{x}_0$ being selected to 0 is always looked for when the corresponding exponent of the monomial is the highest. The situations in which faces or edges are parallel to the global axes are also taken into account, through a proper tolerance: in these

[1] A quadrature-free integration scheme does not adopt integration points, exploiting only analytical-type evaluations of the geometry of the domain of integration.

Table 1
Numerical integration formulae for tetrahedra

degree of precision	number of integral points	tetrahedral coordinates	weights
1	1	1/4, 1/4, 1/4, 1/4	1
2	4	a, b, b, b	1/4
		b, a, b, b	1/4
		b, b, a, b	1/4
		b, b, b, a	1/4
		with	
		$a = \left(5 + 3\sqrt{5}\right)/4$	
		$b = \left(5 - 3\sqrt{5}\right)/4$	
3	5	1/4, 1/4, 1/4, 1/4	-4/5
		1/2, 1/6, 1/6, 1/6	9/20
		1/6, 1/2, 1/6, 1/6	9/20
		1/6, 1/6, 1/2, 1/6	9/20
		1/6, 1/6, 1/6, 1/2	9/20
4	11	1/4, 1/4, 1/4, 1/4	-148/1875
		11/14, 1/14, 1/14, 1/14	343/7500
		1/14, 11/14, 1/14, 1/14	343/7500
		1/14, 1/14, 11/14, 1/14	343/7500
		1/14, 1/14, 1/14, 11/14	343/7500
		a, a, b, b	56/375
		a, b, a, b	56/375
		a, b, b, a	56/375
		b, a, a, b	56/375
		b, a, b, a	56/375
		b, b, a, a	56/375
		with	
		$a = \left(1 + \sqrt{5/14}\right)/4$	
		$b = \left(1 - \sqrt{5/14}\right)/4$	

Table 2
Numerical integration formulae for triangles

degree of precision	number of integral points	triangular coordinates	weights
1	1	1/3, 1/3, 1/3	1
2	3	1/2, 1/2, 0	1/3
		1/2, 0, 1/2	1/3
		0, 1/2, 1/2	1/3
3	4	1/3, 1/3, 1/3	-27/48
		3/5, 1/5, 1/5	25/48
		1/5, 3/5, 1/5	25/48
		1/5, 1/5, 3/5	25/48

cases, there is no arbitrariness in the choice of $\boldsymbol{x}_0$.

Table 3
The number of integral points in the numerical application

strain model	$\boldsymbol{G}$ matrix	$\boldsymbol{E}$ matrix	$\boldsymbol{F}_e$ matrix	$\boldsymbol{A}_1$ matrix
constant strain model	1×6	1×6	1×6	1×12
linear strain model	4×6	4×6	4×6	3×12
quadratic strain model	11×6	11×6	11×6	4×12

3.4. Numerical check of element stability in regular and distorted configurations

Proving that the stiffness matrix $\boldsymbol{K}_e^c$ generated by the quadratic strain models presented in Section 3.2 has the correct rank deficiency, and hence the elements require no stabilization, is an extremely difficult task. A rigorous stability analysis of self-stabilized VEs has been provided in [40] for the simpler case of 2D quadrilateral $k = 1$ VEs. However, for 2D polygons with more than four edges or for 3D VEs, such an analysis is still missing.

To state that the considered deltahedral 3D VEs can be safely used, excluding the possibility of the development of spurious zero-energy modes, their stiffness matrices $\boldsymbol{K}_e^c$ should have, up to machine precision, exactly six null eigenvalues corresponding to the rigid body motions in 3D, but not more than six. In the absence of a theoretical proof, a heuristic approach has been pursued, which however cannot rigorously guarantee stability. Starting from a unit cubic element, its geometry is arbitrarily varied by moving its nodes. A numerical optimization is then performed with respect to the nodes' positions to find the element configuration leading to the closest-to-zero 7^{th} smallest eigenvalue. This search is non-trivial, as the convexity of the corresponding objective function is not guaranteed, and preserving the element's topology (i.e., the element faces should not degenerate, and its vertices should not penetrate other faces) is challenging. The following optimization problem has been implemented using the MATLAB Optimization Toolbox ([41]).

$$\text{Find} \quad \min_{\boldsymbol{x} \in \mathbb{R}^{24}} f(\boldsymbol{x}) \quad \text{s.t. } g(\boldsymbol{x}) \leq 0 \tag{32}$$

where $f(\boldsymbol{x})$ is the objective function taking as input the variation $\boldsymbol{x}$ of coordinates of the eight vertices with respect to the initial configuration of the unit cubic element, and returning the square of the 7^{th} smallest eigenvalue of the generated stiffness matrix $\boldsymbol{K}_e^c$. The material properties are Young's modulus $E = 1$ and Poisson ratio $\nu = 0.25$. To prevent triangle degeneration and penetration of faces, a set of constrains has been imposed. In particular, it should be guaranteed that the area of each of the twelve triangles remains strictly positive, imposing in this way a constraint on the variation $\boldsymbol{x}$ of nodal coordinates. To enforce the correct signed area, the scalar product between the area vector of the deformed triangles and the area vector of the undeformed triangles is imposed to be positive. The non-linear

Table 4
Eigenvalues for the stiffness matrix $\boldsymbol{K}_e^c$.

Eigenvalue	ΔVEM8SS31-24DOFs		ΔVEM8SS25-24DOFs		ΔVEM8SS18-24DOFs	
	Reference	Optimized	Reference	Optimized	Reference	Optimized
λ_{1-6}	$\sim 10^{-16}$	$\sim 10^{-16}$	$\sim 10^{-16}$	$\sim 10^{-16}$	$\sim 10^{-16}$	$\sim 10^{-16}$
λ_7	0.1184	0.00066	0.0560	0.00044	0.1474	0.00008
λ_{24}	2.9007	46.9519	2.9012	8.0323	2.8621	9.3202

constraints $g(\boldsymbol{x})$ reads:

$$g(\boldsymbol{x}) = g_f(\boldsymbol{x}_i, \boldsymbol{x}_j, \boldsymbol{x}_k) = -[\underbrace{((\boldsymbol{r}_j + \boldsymbol{x}_j) - (\boldsymbol{r}_i + \boldsymbol{x}_i)) \times ((\boldsymbol{r}_k + \boldsymbol{x}_k) - (\boldsymbol{r}_i + \boldsymbol{x}_i))}_{\text{area vector of distorted triangle}}] \cdot [\ \underbrace{(\boldsymbol{r}_j - \boldsymbol{r}_i) \times (\boldsymbol{r}_k - \boldsymbol{r}_i)}_{\text{area vector of original triangle}}\ ] \tag{33}$$

$$\forall \text{ triangular face } f \text{ with vertices } i, j, k \in f \tag{34}$$

where $\boldsymbol{r}_i$ represents the original position of vertex i and $\boldsymbol{r}_i + \boldsymbol{x}_i$ its position in the distorted configuration. Fig. 6 shows the reference configuration of the deltahedral VE whose stiffness matrix $\boldsymbol{K}_e^c$ has been analyzed, and the three configurations corresponding to the solutions of the optimization problem in Eq.(32) for the three self-stabilized virtual elements. Table 4 displays the first six smallest eigenvalues, the 7^{th} and, as a comparative measure, the largest one for the three self-stabilized virtual elements in the reference and optimized (i.e., most unfavourable from the point of view of stability) configurations. The three proposed quadratic strain models produce a local stiffness matrix $\boldsymbol{K}_e^c$, which exhibits only six null eigenvalues corresponding to the rigid body motions, yielding a partial validation of the elements.

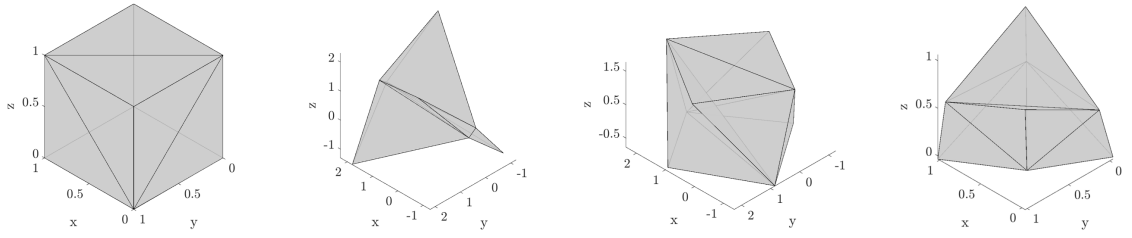

(a) Reference (b) Optimized for ΔVEM8SS31-24DOFs (c) Optimized for ΔVEM8SS25-24DOFs (d) Optimized for ΔVEM8SS18-24DOFs

Fig. 6: Reference configuration and configurations leading to the closest-to-zero 7^{th} smallest eigenvalue of the stiffness matrix $\boldsymbol{K}_e^c$ generated by the 31-, 25-, and 18-parameters strain models.

4. Numerical applications

The 3D VEM with the proposed deltahedral elements has been implemented into an in-house MATLAB code, and several numerical applications have been conducted to evaluate its performance for various types of elements.

4.1. Convergence tests with analytical solution

A convergence test with a known analytical solution has been carried out to assess the convergence rate of deltahedral VEs with a regular or a highly distorted configuration. The problem domain is a unit cube $\Omega = [0,1]^3$ with constrained displacements all over its boundary $\partial_u\Omega \equiv \partial\Omega$. The data for the problem are as follows:

(i) Lamé constants $\lambda = 1$ and $\mu = 1$ (corresponding to modulus $E = 2.5$, Poisson's ratio $\nu = 0.25$)

(ii) body force in Ω

$$b_x = -\pi^2 \left[-(\lambda+4\mu)\sin(\pi x)\sin(\pi y)\sin(\pi z) + (\lambda+\mu)\cos(\pi x)\cos(\pi y)\sin(\pi z) + (\lambda+\mu)\cos(\pi x)\sin(\pi y)\cos(\pi z)\right] \tag{35}$$

$$b_y = -\pi^2 \left[-(\lambda+4\mu)\sin(\pi x)\sin(\pi y)\sin(\pi z) + (\lambda+\mu)\cos(\pi x)\cos(\pi y)\sin(\pi z) + (\lambda+\mu)\sin(\pi x)\cos(\pi y)\cos(\pi z)\right] \tag{36}$$

$$b_z = -\pi^2 \left[-(\lambda+4\mu)\sin(\pi x)\sin(\pi y)\sin(\pi z) + (\lambda+\mu)\cos(\pi x)\sin(\pi y)\cos(\pi z) + (\lambda+\mu)\sin(\pi x)\cos(\pi y)\cos(\pi z)\right] \tag{37}$$

(iii) boundary conditions on $\partial_u\Omega \equiv \partial\Omega$

$$\bar{u}_x = \bar{u}_y = \bar{u}_z = 0 \tag{38}$$

The analytical solution to the problem in terms of displacements in Ω is given by:

$$u_x = u_y = u_z = \sin(\pi x)\sin(\pi y)\sin(\pi z) \tag{39}$$

which yields the following strain field:

$$\varepsilon_{xx} = \pi\cos(\pi x)\sin(\pi y)\sin(\pi z) \tag{40}$$

$$\varepsilon_{yy} = \pi\sin(\pi x)\cos(\pi y)\sin(\pi z) \tag{41}$$

$$\varepsilon_{zz} = \pi\sin(\pi x)\sin(\pi y)\cos(\pi z) \tag{42}$$

$$\varepsilon_{xy} = \pi\left[\sin(\pi x)\cos(\pi y)\sin(\pi z) + \cos(\pi x)\sin(\pi y)\sin(\pi z)\right] \tag{43}$$

$$\varepsilon_{yz} = \pi \left[\sin(\pi x)\sin(\pi y)\cos(\pi z) + \sin(\pi x)\cos(\pi y)\sin(\pi z)\right] \tag{44}$$

$$\varepsilon_{zx} = \pi \left[\cos(\pi x)\sin(\pi y)\sin(\pi z) + \sin(\pi x)\sin(\pi y)\cos(\pi z)\right] \tag{45}$$

The different strain models proposed in Section 3.2 have been tested for the assessment of VEM convergence when increasing the number of elements, for two different types of meshes: a mesh of parallelepipeds and a mesh of distorted elements. In particular, we have investigated distortions of two opposite faces of the brick-like Deltahedron, while the other four sides remain rectangular (and planar). Additionally, we have evaluated the impact of the element Thickness Ratio (TR), defined by the ratio of element thickness to length, on convergence and accuracy. Convergence upon mesh refinement has been assessed in terms of the L^2-norm of the strain error, defined as:

$$\left\|e_\varepsilon\right\| = \sqrt{\sum_{e=1}^{n_e} \int_{\Omega_e} \left\|\boldsymbol{\varepsilon} - \boldsymbol{\varepsilon}^h\right\|^2 d\Omega} \tag{46}$$

where ε denotes the exact strain over the generic VE, and ε^h denotes the approximate strain defined in (9). Eq.(46) is numerically integrated using the same technique and the same Gaussian points adopted for calculating the element compatibility matrix $\boldsymbol{G}$.

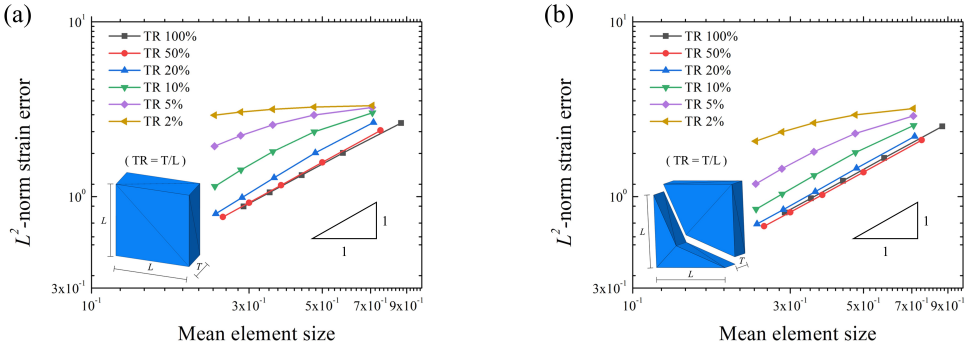

Fig. 7: Convergence curves of deltahedral elements with constant strain model in Eq.(25): (a) regular brick elements, (b) distorted elements.

To compare the performance of these deltahedral elements, we plotted the L^2-norm strain error $\left\|e_\varepsilon\right\|$ on a log-log scale against the mean element size h_e. The slope of the error curve should tend to the order of approximation $k = 1$ of the method. Fig. 7 shows the convergence curves of regular brick and distorted elements with the constant strain model. In both cases, the strain error increases as the element becomes thinner, indicating a decrease in accuracy. It is observed that the brick elements with a thickness ratio of 10% or more exhibit the expected convergence rates. Distorted elements perform better and show linear convergence rates, except for the element with a thickness ratio of 2%.

Fig. 8 shows the convergence curves of brick-like distorted elements with the quadratic strain model shown in Eq.

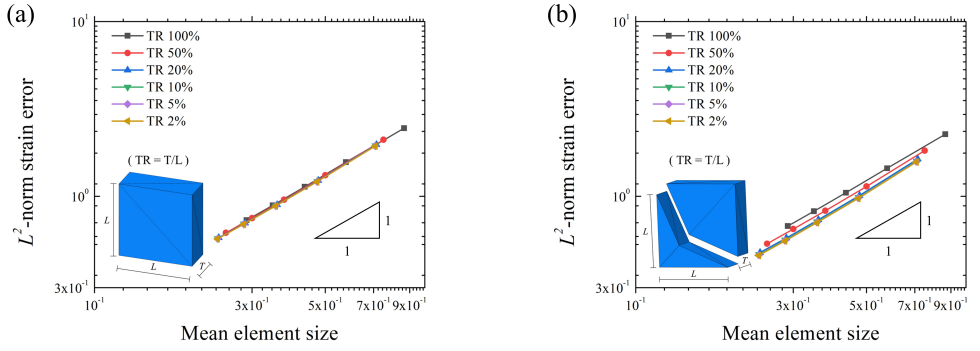

Fig. 8: Convergence curves of ΔVEM8SS31-24DOFs elements with quadratic strain model in Eq. (29): (a) regular brick elements, (b) distorted elements.

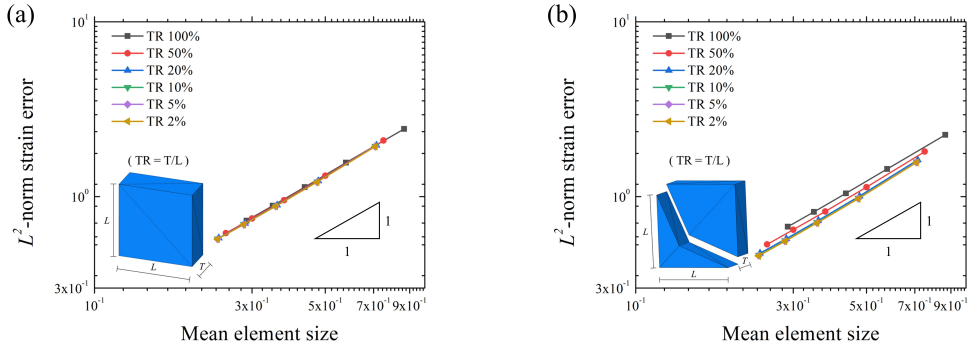

Fig. 9: Convergence curves of ΔVEM8SS25-24DOFs elements with quadratic strain model in Eq. (30): (a) regular brick elements, (b) distorted elements.

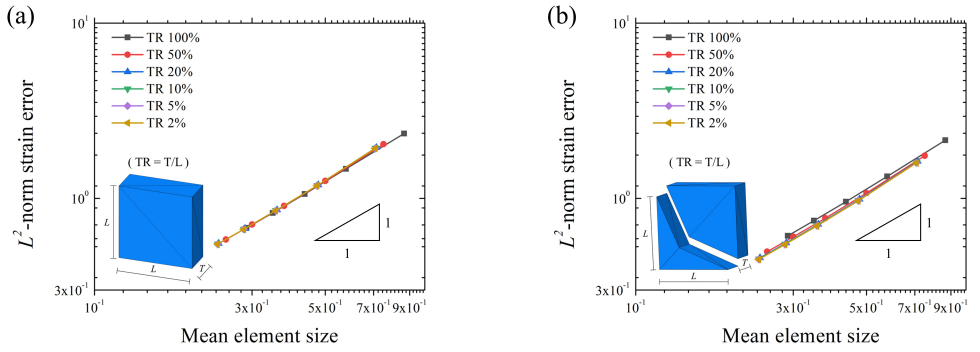

Fig. 10: Convergence curves of ΔVEM8SS18-24DOFs elements with quadratic strain model in Eq. (31): (a) regular brick elements, (b) distorted elements.

(29). In this problem, the regular brick-like deltahedral elements exhibit excellent thickness independence, displaying optimal convergence rates and the same level of accuracy for all thickness ratios. The distorted elements also exhibit the expected convergence rate for each thickness ratio, but their accuracy slightly declines as the element gets thinner. Fig. 9 and Fig. 10 illustrate the convergence curves of regular brick elements and distorted elements with quadratic strain model, and 25 and 18 parameters, shown in Eq. (30) and Eq. (31), respectively, showing the expected convergence rate in each case.

4.2. Comparison against FEM in structural examples

We report here the results for two structural problems solved with the newly presented self-stabilized ΔVEMs and compare them with standard FE analyses performed with ABAQUS ([42]) and 8-node brick elements. Note that meshes entirely made of VEs have been considered for both problems for comparison purposes, to highlight the differences with respect to the FEM. In practice, however, as already mentioned, VEs are intended to be introduced in a mesh of FEs only where it is necessary, to locally solve meshing problems, otherwise difficult to solve with standard FEs.

The first considered problem consists of a cantilever beam under self-weight, modeled as a uniformly distributed load, as shown in Fig. 11. The deltahedral mesh adopted for the ΔVEMs is displayed in Fig. 12. A structured mesh of 8-node brick FEs having the same total nodal DOFs is employed for the standard FEM solution.

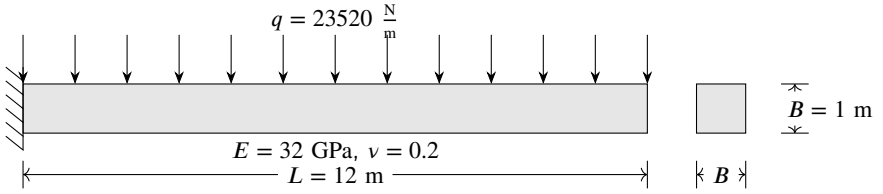

Fig. 11: Cantilever beam under self-weight. Geometry, boundary conditions loading and material property.

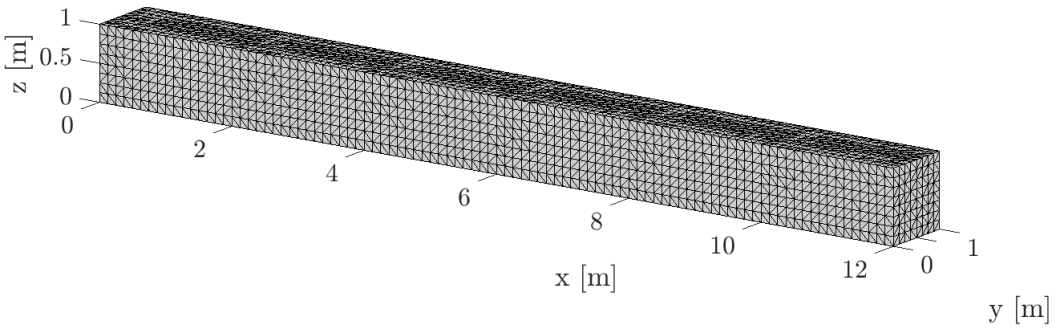

Fig. 12: Cantilever beam under self-weight. Mesh of 23571 DOFs and 6144 ΔVEs. The clamped end is on the yz plane at $x = 0$.

The maximum vertical displacements found are summarized in Table 5. All the proposed schemes lead to a maximum vertical displacement very close to the one obtained with the standard FEM.

The second structural problem is a simply supported square plate under self-weight, modeled as a uniformly distributed load, as shown in Figure 13. The deltahedral mesh adopted for the ΔVEMs is displayed in Fig. 14. A structured mesh of 8-node brick FEs having the same total number of DOFs is employed for the standard FEM analysis.

The maximum vertical displacement found is summarized in Table 6.

It is noted that for the cantilever beam, the self-stabilized ΔVEMs substantially predict the same displacements of

Table 5
Cantilever beam under self-weight. Maximum vertical displacement for self-stabilized ΔVEs and FEM brick elements.

Method	$\delta_{\max}$ [m]
ΔVEM8SS31-24DOFs	0.02273
ΔVEM8SS25-24DOFs	0.02274
ΔVEM8SS18-24DOFs	0.02289
C3D8 FE	0.02289

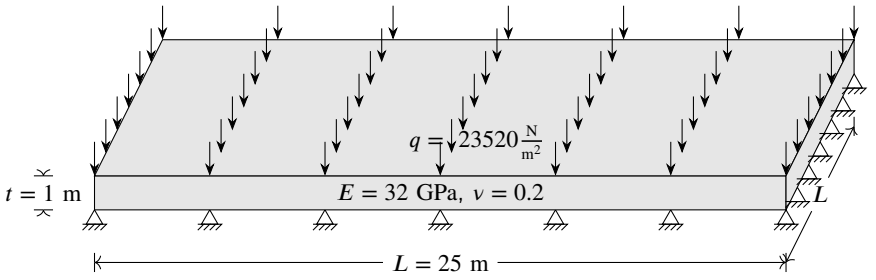

Fig. 13: Simply supported square plate under uniformly distributed load. Geometry, boundary conditions, loading and material properties.

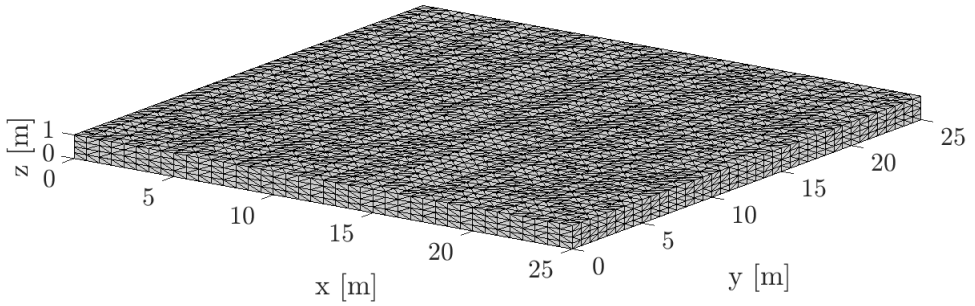

Fig. 14: Simply supported square plate under uniformly distributed load. Mesh of 25215 DOFs and 6400 ΔVEs.

Table 6
Simply supported square plate under uniformly distributed load. Maximum vertical displacement for self-stabilized ΔVEs and FEM brick elements.

Method	$\delta_{\max}$ [m]
ΔVEM8SS31-24DOFs	0.01183
ΔVEM8SS25-24DOFs	0.01199
ΔVEM8SS18-24DOFs	0.01338
C3D8 FE	0.01344

the standard FEM. As for the plate, however, the first two self-stabilized strain schemes, leading to internally redundant models, seem to produce a slightly stiffer system, while the ΔVEM8SS18-24DOFs behaves very similarly to the standard 8-node brick element.

Table 7
Integral values and average computational times over 100 trials for standard Gauss integration applied to the subdivision of the deltahedron in tetrahedra, and for the quadrature-free algorithm.

Monomial integrand	Quadrature-free		Gauss	
	Integral	Computational time	Integral	Computational time
1	1.000000000000000	0.0007	1.000000000000000	0.0053
ξ	0.500000000000000	0.0013	0.500000000000000	0.0049
ξ^2	0.333333333333333	0.0022	0.333333333333333	0.0056
ξ^3	0.250000000000000	0.0030	0.250000000000000	0.0064
ξ^4	0.200000000000000	0.0045	0.200000000000000	0.0063
$\xi^3\eta$	0.125000000000000	0.0124	0.125000000000000	0.0061
$\xi^2\eta^2$	0.111111111111111	0.0170	0.111111111111111	0.0057
$\xi\eta^3$	0.125000000000000	0.0120	0.125000000000000	0.0058
η^4	0.200000000000000	0.0040	0.200000000000000	0.0063
$\xi^2\eta\zeta$	0.0833333333333333	0.0383	0.0833333333333333	0.0068
$\xi\eta^2\zeta$	0.0833333333333333	0.0391	0.0833333333333333	0.0066
$\xi\eta\zeta^2$	0.0833333333333333	0.0378	0.0833333333333333	0.0067

4.3. Comparison of computational efficiency of different integration schemes

We report here a comparison of the computational efficiency for the integration algorithms presented in Section 3.3, applied to exactly integrate a monomial up to degree 4, as is the case for the proposed self-stabilized ΔVEMs, over the unit cubic Deltahedron of Fig. 6(a). Table 7 summarizes the average computational times computed over 100 trials, required by standard Gauss integration applied to the tetrahedra obtained by subdivision of the Deltahedron, and those required by the quadrature-free algorithm described in Section 3.3 for the given monomial integrands. For the 8-node deltahedral element, the quadrature-free formula is generally faster than Gauss integration if the integrand is a monomial containing only one single variable whose exponent is non-zero. This is due to the recursive call the algorithm has to go through when a non-zero exponent is present. We remark that adopting the quadrature-free algorithm may be convenient when dealing with complex, non-convex, polyhedral meshes, where the internal subdivision with tetrahedra can be particularly costly. Even if the method allows for integration over non-convex elements, for the purpose of the presented self-stabilized ΔVEMs, Gauss integration seems to be more efficient and applicable as 8-nodes deltahedra are always star-shaped, allowing for a rather simple internal subdivision.

5. Conclusions

3D finite element meshes with first-order 8-node brick elements are commonly employed for the analysis of 3D engineering problems. Depending on the complexity of the geometry to be modeled, the construction of these meshes may not be easy, with regions of highly distorted bricks that need a specific treatment. In this work, it has been shown how a possible remedy to this difficulty is the local use of distortion-insensitive first-order polyhedral VEs, which can be smoothly integrated into finite element meshes.

To this purpose, a new type of self-stabilized 3D polyhedral VEs with triangular faces, named *Deltahedra*, has been proposed. The main feature of these elements is that the displacement field on their faces is explicitly defined by nodal values. Special attention has been devoted to $k = 1$ brick-like 8-node, 12-face, VEs, which can be easily coupled to planar faces of 8-node FEs. Following the approach in [8], the deltahedral element has been derived starting from a mixed Hu-Washizu variational formulation, allowing for independent modeling of the strain field. Other notable features of the considered Deltahedra are:

- to arrive at a self-stabilized VE, quadratic strain models, based on a sufficient number of strain parameters, have been considered;
- to avoid the need for additional *moment* DOFs, three different div-free second-order strain models have been analyzed: the first, employing 31 strain parameters, is derived from a complete fourth-order polynomial using Airy's technique to construct div-free tensor fields; the second, employing 25 strain parameters is obtained by application to a complete fourth-order polynomial of the *incompatibility* operator of the differential complex theory for elasticity problems, producing a div-free strain tensor with second-order polynomial components that are also the symmetric gradient of a vector field; the third second order div-free strain model, employing 18 strain parameters (the minimum needed for element stability) is empirically obtained by combining the columns of the previous models;
- being obtained by frame invariant, coordinate-free operations, the first two models give rise to strain fields that transform as second order tensors, ensuring the element frame invariance; the third strain model is not frame invariant unless it is formulated with respect to a co-rotational intrinsic reference frame;
- the stability of the proposed VEs has been numerically verified by computing the lowest eigenvalue of the stiffness matrix for the most unfavourable distortion.
- an integration scheme based on quadrature and an alternative quadrature-free scheme have been investigated and comparatively assessed for the integration of the higher order polynomial terms arising from the second order strain models.

The numerical tests have confirmed the distortion insensitivity and first-order convergence rate of the considered VEs. As expected, the element with 18 strain parameters, i.e. the minimum number required to guarantee element stability, has proved to perform better in terms of accuracy than the internally redundant ones, with 31 and 25 strain parameters. The feasibility of the local use of VEs in a FE mesh has also been confirmed.

Acknowledgements

This research was partially supported by the Italian Ministry of University and Research through the project PRIN2022 PNRR "Polyhedral Galerkin methods for engineering applications to improve disaster risk forecast and management: stabilization-free operator preserving methods and optimal stabilization methods" (PRIN2022 PNRR - P2022BH5CB, CUP D53D23018840001: UE funding – NextGenerationEU – mission 4, component 2, investment 1.1). C.L. and A.R. are members of the INdAM Research group GNCS and they were partially supported by INdAM-GNCS and the Italian MUR (Ministero dell'Università e della Ricerca) through the Projects PRIN2020 "Advanced polyhedral discretizations of heterogeneous PDEs for multiphysics problems". Qun Li was supported by the National Natural Science Foundation of China (Nos.12172270).

References

[1] O.C. Zienkiewicz, R.L. Taylor, and J.Z. Zhu. *The finite element method: its basis and fundamentals*. Elsevier, 2005.

[2] L. Beirão da Veiga, F. Brezzi, A. Cangiani, G. Manzini, L.D. Marini, and A. Russo. Basic principles of virtual element methods. *Mathematical Models and Methods in Applied Sciences*, 23(01):199–214, 2013.

[3] L. Beirão Da Veiga, F. Brezzi, and L.D. Marini. Virtual elements for linear elasticity problems. *SIAM Journal on Numerical Analysis*, 51(2): 794–812, 2013.

[4] A.L. Gain, C. Talischi, and G.H. Paulino. On the virtual element method for three-dimensional linear elasticity problems on arbitrary polyhedral meshes. *Computer Methods in Applied Mechanics and Engineering*, 282:132–160, 2014.

[5] E. Artioli, L. Beirão da Veiga, C. Lovadina, and E. Sacco. Arbitrary order 2D virtual elements for polygonal meshes: part I, elastic problem. *Computational Mechanics*, 60:355–377, 2017.

[6] E Artioli, S De Miranda, C Lovadina, and L Patruno. A stress/displacement virtual element method for plane elasticity problems. *Computer Methods in Applied Mechanics and Engineering*, 325:155–174, 2017.

[7] E. Artioli, S. de Miranda, C. Lovadina, and L. Patruno. A family of virtual element methods for plane elasticity problems based on the hellinger–reissner principle. *Computer Methods in Applied Mechanics and Engineering*, 340:978–999, 2018.

[8] A. Lamperti, M. Cremonesi, U. Perego, A. Russo, and C. Lovadina. A Hu–Washizu variational approach to self-stabilized virtual elements: 2D linear elastostatics. *Computational Mechanics*, 71(5):935–955, 2023.

[9] K. Park, H. Chi, and G.H. Paulino. On nonconvex meshes for elastodynamics using virtual element methods with explicit time integration. *Computer Methods in Applied Mechanics and Engineering*, 356:669–684, 2019.

[10] K. Park, H. Chi, and G.H. Paulino. Numerical recipes for elastodynamic virtual element methods with explicit time integration. *International Journal for Numerical Methods in Engineering*, 121(1):1–31, 2020.

[11] P.F. Antonietti, G. Manzini, I. Mazzieri, H.M. Mourad, and M. Verani. The arbitrary-order virtual element method for linear elastodynamics models: convergence, stability and dispersion-dissipation analysis. *International Journal for Numerical Methods in Engineering*, 122(4): 934–971, 2021.

[12] A. Lamperti, M. Cremonesi, U. Perego, A. Russo, and C. Lovadina. A Hu-Washizu variational approach to self-stabilized quadrilateral Virtual Elements: 2D linear elastodynamics. *Computational Mechanics*, 74(2):393–415, feb 2024. ISSN 14320924. doi: 10.1007/S00466-023-02438-0.

[13] P. Wriggers, W.T. Rust, and B.D. Reddy. A virtual element method for contact. *Computational Mechanics*, 58:1039–1050, 2016.

[14] E. Artioli, S. Marfia, and E. Sacco. VEM-based tracking algorithm for cohesive/frictional 2D fracture. *Computer Methods in Applied Mechanics and Engineering*, 365:112956, 2020.

[15] M. Cihan, B. Hudobivnik, J. Korelc, and P. Wriggers. A virtual element method for 3D contact problems with non-conforming meshes. *Computer Methods in Applied Mechanics and Engineering*, 402:115385, 2022.

[16] W. Shen, M. Ohsaki, and J. Zhang. A 2-dimentional contact analysis using second-order virtual element method. *Computational Mechanics*, 70(2):225–245, 2022.

[17] V.M. Nguyen-Thanh, X. Zhuang, H. Nguyen-Xuan, T. Rabczuk, and P. Wriggers. A virtual element method for 2D linear elastic fracture analysis. *Computer Methods in Applied Mechanics and Engineering*, 340:366–395, 2018.

[18] F. Aldakheel, B. Hudobivnik, A. Hussein, and P. Wriggers. Phase-field modeling of brittle fracture using an efficient virtual element scheme. *Computer Methods in Applied Mechanics and Engineering*, 341:443–466, 2018.

[19] E. Benvenuti, A. Chiozzi, G. Manzini, and N. Sukumar. Extended virtual element method for two-dimensional linear elastic fracture. *Computer Methods in Applied Mechanics and Engineering*, 390:114352, 2022.

[20] T.-R. Liu, F. Aldakheel, and M.H. Aliabadi. Virtual element method for phase field modeling of dynamic fracture. *Computer Methods in Applied Mechanics and Engineering*, 411:116050, 2023.

[21] P. Wriggers, F. Aldakheel, and B. Hudobivnik. *Virtual Element Methods in Engineering Sciences*. Springer International Publishing, 2024. doi: 10.1007/978-3-031-39255-9.

[22] L. Beirão Da Veiga, F. Brezzi, L.D. Marini, and A. Russo. The virtual element method. *Acta Numerica*, 32:123–202, may 2023. ISSN 0962-4929. doi: 10.1017/S0962492922000095.

[23] E. Benvenuti, A. Chiozzi, G. Manzini, and N. Sukumar. Extended virtual element method for the laplace problem with singularities and discontinuities. *Computer Methods in Applied Mechanics and Engineering*, 356:571–597, 2019.

[24] A. Cangiani, G. Manzini, A. Russo, and N. Sukumar. Hourglass stabilization and the virtual element method. *International Journal for Numerical Methods in Engineering*, 102(3-4):404–436, 2015.

[25] P. Wriggers, B.D. Reddy, W. Rust, and B36844961386 Hudobivnik, B. Efficient virtual element formulations for compressible and incompressible finite deformations. *Computational Mechanics*, 60:253–268, 2017.

[26] A.M. D'Altri, S. de Miranda, L. Patruno, and E. Sacco. An enhanced VEM formulation for plane elasticity. *Computer Methods in Applied Mechanics and Engineering*, 376:113663, 2021.

[27] L. Mascotto. The role of stabilization in the virtual element method: A survey. *Computers & Mathematics with Applications*, 151:244–251, dec 2023. ISSN 0898-1221. doi: 10.1016/J.CAMWA.2023.09.045.

[28] T. Belytschko, J.S.-J. Ong, W.K. Liu, and J.M. Kennedy. Hourglass control in linear and nonlinear problems. *Computer methods in applied mechanics and engineering*, 43(3):251–276, 1984.

[29] A. Chen and N. Sukumar. Stabilization-free serendipity virtual element method for plane elasticity. *Computer Methods in Applied Mechanics and Engineering*, 404:115784, 2023. doi: 10.1016/J.CMA.2022.115784.

[30] Stefano Berrone, Andrea Borio, and Francesca Marcon. A stabilization-free virtual element method based on divergence-free projections. *Computer Methods in Applied Mechanics and Engineering*, 424:116885, 5 2024. ISSN 0045-7825. doi: 10.1016/J.CMA.2024.116885.

[31] B.B. Xu and P. Wriggers. 3D stabilization-free virtual element method for linear elastic analysis. *Computer Methods in Applied Mechanics and Engineering*, 421:116826, mar 2024. ISSN 0045-7825. doi: 10.1016/J.CMA.2024.116826.

[32] F. Dassi and L. Mascotto. Exploring high-order three dimensional virtual elements: Bases and stabilizations. *Computers & Mathematics with*

Applications, 75(9):3379–3401, may 2018. ISSN 0898-1221. doi: 10.1016/J.CAMWA.2018.02.005.

[33] H. Haichang. On some variational principles in the theory of elasticity and the theory of plasticity. *Acta Physica Sinica*, 10(3):259–290, 1954.

[34] K. Washizu. *On the variational principles of elasticity and plasticity*. MIT Aeroelastic and Structures Research Laboratory Cambridge, UK, 1955.

[35] S.H. Christiansen, K. Hu, and E. Sande. Poincaré path integrals for elasticity. *Journal de Mathématiques Pures et Appliquées*, 135:83–102, 2020. ISSN 0021-7824. doi: https://doi.org/10.1016/j.matpur.2019.06.002. URL https://www.sciencedirect.com/science/article/pii/S0021782419301187.

[36] F.S. Liguori, A. Madeo, S. Marfia, and E. Sacco. A hybrid virtual element formulation for 2D elasticity problems. *Computer Methods in Applied Mechanics and Engineering*, 426:116970, June 2024. ISSN 00457825. doi: 10.1016/j.cma.2024.116970. URL https://linkinghub.elsevier.com/retrieve/pii/S0045782524002263.

[37] M. Nale, C. Gatta, D. Addessi, E. Benvenuti, and E. Sacco. An enhanced corotational Virtual Element Method for large displacements in plane elasticity. *Computational Mechanics*, 74(2):379–392, August 2024. ISSN 1432-0924. doi: 10.1007/s00466-023-02437-1. URL https://doi.org/10.1007/s00466-023-02437-1.

[38] J.E. Akin. *Finite element analysis with error estimators: An introduction to the FEM and adaptive error analysis for engineering students*. Elsevier, 2005.

[39] P.F. Antonietti, P. Houston, and G. Pennesi. Fast numerical integration on polytopic meshes with applications to discontinuous Galerkin finite element methods. *Journal of Scientific Computing*, 77(3):1339–1370, 2018.

[40] M. Cremonesi, A. Lamperti, C. Lovadina, U. Perego, and A. Russo. Analysis of a stabilization-free quadrilateral Virtual Element for 2D linear elasticity in the Hu-Washizu formulation. *Computers & Mathematics with Applications*, 155:142–149, 2024. ISSN 08981221. doi: 10.1016/j.camwa.2023.12.001.

[41] The MathWorks Inc. Matlab version: 9.13.0 (r2022b), 2022. URL https://www.mathworks.com.

[42] M. Smith. *ABAQUS/Standard User's Manual, Version 6.9*. Dassault Systèmes Simulia Corp, United States, 2009.